



Original Paper

Perforation optimization of layer-penetration fracturing for commingling gas production in coal measure strata

Bing Hou^{a, b, *}, Zhuang Cui^{a, b}, Ji-Hui Ding^c, Feng-Shou Zhang^d, Li Zhuang^e,
Derek Elsworth^f

^a State Key Laboratory of Petroleum Resources and Prospecting, China University of Petroleum-Beijing, Beijing, 102249, China

^b MOE Key Laboratory of Petroleum Engineering in China University of Petroleum, Beijing 102249, China

^c Department of Geophysics, Stanford University, 397 Panama Mall, Stanford, CA, 94305, USA

^d Department of Geotechnical Engineering, Tongji University, Shanghai, 200092, China

^e Korea Institute of Civil Engineering and Building Technology, Goyang, 10223, South Korea

^f The Pennsylvania State University, University Park, PA, 16802, USA



ARTICLE INFO

Article history:

Received 27 September 2021

Received in revised form

7 March 2022

Accepted 10 March 2022

Available online 15 March 2022

Edited by Yan-Hua Sun

Keywords:

Coal measure strata

Combined production

3D lattice algorithm

Perforation scheme optimization

Fracture propagation

ABSTRACT

Optimization of fracturing perforation is of great importance to the commingling gas production in coal measure strata. In this paper, a 3D lattice algorithm hydraulic fracturing simulator was employed to study the effects of perforation position and length on hydraulic fracture propagation in coal measures of the Lin-Xing block, China. Based on field data, three lithologic combinations are simulated: 1) a thick section of coal seam sandwiched by sandstones; 2) a thin coal seam layer overlay by gas-bearing tight sandstone; 3) two coal seams separated by a thin layer of sandstone. Our simulation shows that perforation position and length in multi-layer reservoirs play a major role in hydraulic fracture propagation. Achieving maximum stimulated volume requires consideration of lithologic sequence, coal seam thickness, stress states, and rock properties. To improve the combined gas production in coal measure strata, it is possible to simultaneously stimulate multiple coal seams or adjacent gas-bearing sandstones. In these cases, perforation location and length also significantly impact fracture propagation, and therefore should be carefully designed. Our simulation results using 3D lattice algorithm are qualitatively consistent with laboratory physical simulation. 3D lattice models can be used to effectively simulate the fracture propagation through layers in coal measure strata. The numerical results provide guidance for perforation optimization in the hydraulic fracturing of coal measure strata.

© 2022 The Authors. Publishing services by Elsevier B.V. on behalf of KeAi Communications Co. Ltd. This is an open access article under the CC BY-NC-ND license (<http://creativecommons.org/licenses/by-nc-nd/4.0/>).

1. Introduction

Hydraulic fracturing has been widely applied to well stimulation and production enhancement and has achieved great success, especially for the exploration and development of unconventional oil and gas such as shale gas, tight gas and coalbed gas (Fisher et al., 2002; Li et al., 2015; Warpinski et al., 2009). Unconventional oil and gas present unique geological environment and mechanical properties. For example, in unconventional reservoirs, the discontinuity or weak plane significantly affects the propagation of hydraulic fractures (Hou et al., 2013; Zhang et al., 2017). There has been a

great amount of research on the prediction of fracture vertical extension through the layers. Previous studies mainly focused on the interlaminar stress difference (Teufel and Clark, 1984; van Eekelen, 1982), rock mechanical properties (Anderson, 1981; Zhao et al., 2018; Tan et al., 2017a) and interfacial cementation strength (Warpinski and Teufel, 1987; Li et al., 2014). But with the development of unconventional oil and gas, more and more complex engineering problems have challenged the existing theories. For example, the fracturing intervals tend to be thinner and the stratigraphic combination is more abundant, which require a more efficient and reliable simulation method to predict the fracture vertical extension through multi-layers.

Many scholars have studied the fracture propagation in layered formation. Daneshy (1978) firstly carried out the laboratory hydraulic fracturing tests with laminated rock samples, and they

* Corresponding author.

E-mail address: binghou@vip.163.com (B. Hou).

found that the weakly cemented surface can effectively control the expansion of fracture height. Experiments also showed that the *in-situ* stress difference is the main factor affecting the fracture propagation through the layers (Beugelsdijk et al., 2000). Greater stress difference between layers can inhibit vertical expansion of fractures. The viscosity and displacement of fracturing fluid are also the main factors that affect the fracture morphology. A consistent conclusion was drawn that larger viscosity and displacement contribute to fracture vertical expansion (Feng et al., 2016a; Yang et al., 2018). Different from the fracture propagation pattern in the conventional reservoir, the layered formations have unique fracture morphologies, among which, T-type fractures and H-shaped fractures are dominant, and these types of fractures can be formed under unique conditions (Tan et al., 2017b; Wang et al., 2021). The theoretical model of fracture height extension also has made great progress. Based on the fracture mechanics, most studies focused on the stress distribution of cracks in different rocks through fluid-solid coupling to evaluate fracture penetration (Wu et al., 2004). Renshaw and Pollard (1995) established the criteria for fracture propagation across unbounded frictional interfaces through analyzing the discontinuous stress field.

Over the last few decades, numerical analysis such as finite element and discrete element modeling have also been widely applied to study the fracture propagation with a focus on fracture height and aperture (Xing et al., 2018; Chen et al., 2018; Feng et al., 2016b). Most of these numerical simulations are only coupled with aspects of mechanical deformation, fluid flow and fracture propagation, and the dynamic coupling analysis between fracture fluid loss and fracture opening angle is rarely considered. One of the finite element methods is the cohesive element method (Guo et al., 2015) and ABAQUS was used to simulate the fracture height propagation (He et al., 2014). But the finite element method owns some limitations. With the cohesive element method, natural fractures and discontinuities can only be prefabricated before simulation. When using extended finite element method, it is difficult to simulate heterogeneous strata and complex fractured strata. Moreover, the three-dimensional Distinct Element Method Code (3DEC) (Zhang and Dontsov, 2018) and the Rock Failure Process Analysis (RFPA) method (Li et al., 2010) are also widely applied in the fracture simulation in layered formations. Besides, Thallak et al. (1991) used the continuum model to study the vertical extension of hydraulic fractures in loose strata. Potyondy and Cundall (2004) studied the rock cemented particle model, and the mechanical properties of real rock are characterized by cementation between rock particles in the discrete element. The mechanical properties of real rock were further investigated by Sun et al. (2018) using the Discrete Element Method (DEM) and the Bonded Particle Model (BPM). Li et al. (2016) used FEDEM (Finite Element and Discrete Element Combined) to characterize the fracture morphology when it passed through multiple reservoirs in shale. However, most of the discrete element can only calculate a two-dimensional plane, and the computational efficiency for complex fractures in 3D is very low.

To solve these problems, the synthetic rock mass (SRM) approach (Fig. 1) has been developed (Pierce et al., 2007; Ivars et al., 2008). This method includes a bonded particle method and a smooth joint model (SJM) which represent the rock matrix and fractures, respectively. BPM can indicate rock fracture toughness well, and the SJM can characterize shear slip and the opening of the discrete fracture network or faults. The multi-physics options such as fluid flow can be realized by fluid flow in a network of pipes and reservoirs. The SRM method has been realized in PFC2D and PFC3D software and successfully applied to many studies of complex fracture problems, such as the expansion of the fracture height, fluid pressure and the 3D fracture intersection morphology (Owen

et al., 2011; Grassl et al., 2015; Damjanac and Cundall, 2015; Damjanac et al., 2016; Wang et al., 2017).

In this paper, a 3D lattice algorithm hydraulic fracturing simulator XSite (Damjanac et al., 2016) that utilizes the SJM model was employed to simulate the propagation of fractures in representative coal measure strata where the perforation location and length were mainly studied. The lattice-based approach enables a direct and efficient description of the three-dimensional process of hydraulic fracturing. Its reliability has been demonstrated by the applications to various hydraulic fracturing related problems in different engineering geology (Fang and Han, 2018; Zhang et al., 2021). The paper is organized as follows. First, the coal seam stratigraphic combinations and mechanical parameters in the Lin-Xing area of China are selected, and the 3D lattice algorithm is used to simulate fracture propagation in different formation combinations. To promote commingling gas production from multiple coal seams or adjacent gas-bearing sandstones, the focus is given to the effects of perforation location and length on fracturing multiple layers simultaneously. Then, true tri-axial experiments are conducted on the combination of sandstone and coal outcrops to qualitatively verify the accuracy of the numerical simulation results. Our study provides important insights into optimizing fracturing perforation design for stimulating heterogeneous coalbed methane reservoirs.

2. Engineering background

Many fracturing techniques have been developed for fracturing in thin multi-layers of coal measure strata. Just-in-Time-Perforating (JITP) technology was first used in the Pearson basin, America (Adeyeye et al., 2013). Besides, the multi-layer fracturing technology was developed for multiple layer coal seam with intercalation (Li et al., 2006). Due to the well-developed bedding and cleats in the coal seam, sand plugging is the main problem during the fracturing process. The indirect fracturing technology has been developed to solve this problem by fracturing tight sandstone at the top and bottom of the coal seam, to create a longer main fracture and connect the adjacent coal seam, thus increasing the stimulated rock volume (SRV). Worldwide, indirect fracturing was first applied in North America in coalbed methane wells, which reduced the pulverized coal production rate in fracturing and obtained good stimulation results.

In this study, we investigated the hydraulic fracturing for the coal measure strata in the Lin-Xing block, Shanxi Province. The Lin-Xing district is located in Lin County and Xing County, Shanxi Province, northeastern edge of the Ordos Basin. It is a monoclinic structure, primarily composed of fluvial and lacustrine sedimentary facies, where the coal bed gas resources are rich. The coal measures mainly consist of No. 4 + 5 coal seam (average thickness 4.02 m) of Shanxi Formation and No. 8 + 9 coal seam (average thickness 7.2 m) of Benxi Formation. The average depth of coal seam is more than 1500 m. The top and bottom of the coal seam are transition zones, which mainly consist of mudstone, siltstone, and sand-mudstone. There are tight sandstone gas reservoirs and shale gas reservoirs on the top and bottom of the main coal seam, and cycles in the vertical direction (Xie et al., 2015) (Fig. 2). In the early stage of mining, fracturing is carried out for the main thick coal seam and sandstone section separately. Later, commingling production of coalbed methane, shale gas and tight sandstone gas in adjacent thin layers are carried out. But the strong heterogeneity of the strata leads to a rapid decline in production in the fractured area. The main controlling factor of the decline is unknown and requires further study. To improve fracturing efficiency, we employed the 3D lattice algorithm to simulate fracture propagation and studied the effects of perforation position and length in representative formation combinations.

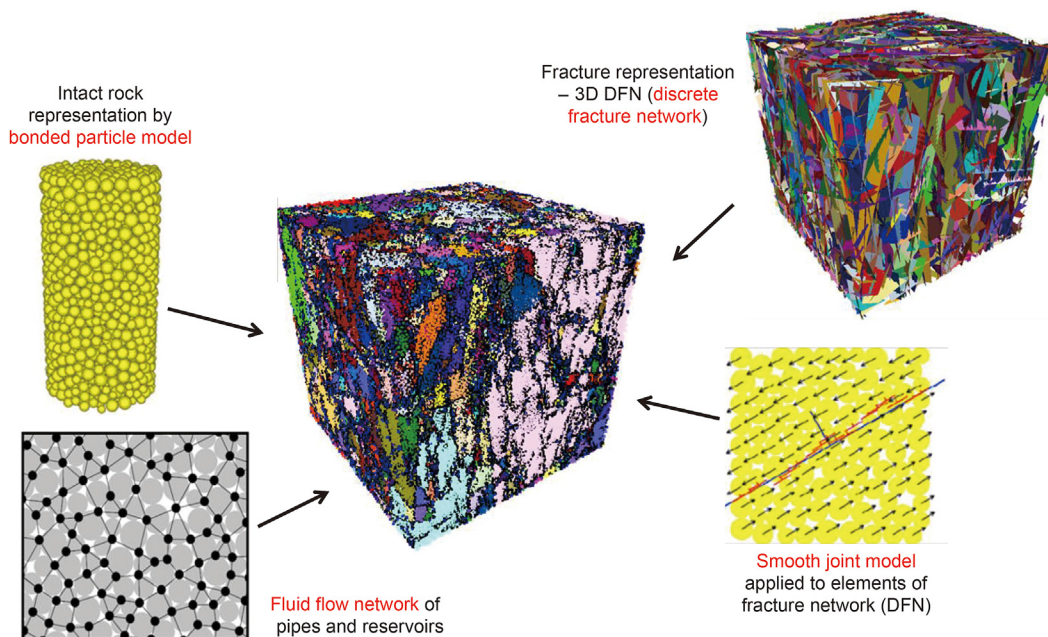


Fig. 1. Schematic diagram of the synthetic rock mass (SRM) approach (Adapted from Damjanac et al., 2016).

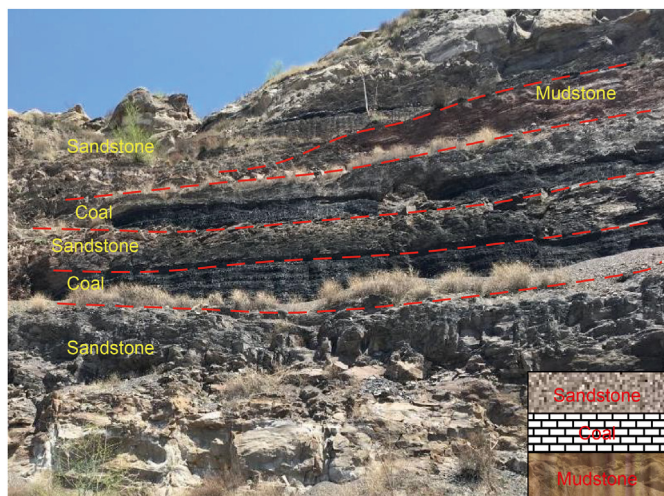


Fig. 2. Sedimentary sequence (sandstone, coal, and mudstone) in the Lin-Xing block and typical stratigraphic combinations based on logging.

3. Numerical modeling methods

3.1. Geometry model

The lattice model in this study fully couples the mechanical responses of fluid flow, fracture propagation and fracturing fluid filtration. All the factors interact with each other and exhibit strong nonlinear behavior. The lattice algorithm is an improvement of the discrete element algorithm, where the rock matrix is represented by spheres in the discrete element model and allows interactions between particles. In the lattice algorithm, the spheres are represented by volume-free particles. The lattice is connected by series of randomly distributed nodes through elastomers. As shown in Fig. 3, the connection between the nodes is similar to the particle cementation algorithm of the discrete element model but with high computing efficiency. When the size of the nodes is smaller than

the whole model, the solid element can be regarded as a continuum to represent the rock. Natural fractures of any sizes and orientations can be inserted into the whole model by breaking the elastomers. The elastomers between nodes can bear both tensile and shear stresses. When the tensile stress between the two joint nodes exceeds the ultimate strength, the elastomer is destroyed. The damaged elastomers appear to be the microcracks in the formation, which ultimately form the macroscopic hydraulic fractures.

3.2. Mechanical model

The mechanical properties are mainly focused on the force and displacement of the joint, the angular velocity of the element and the force analysis of the elastomer. Thus, the law of motion for translational degrees of freedom consists of the following central difference formula:

$$\dot{u}_i^{(t+\Delta t/2)} = \dot{u}_i^{(t-\Delta t/2)} + \Sigma F_i^{(t)} \Delta t / m \tag{1}$$

$$u_i^{(t+\Delta t)} = u_i^{(t)} + \dot{u}_i^{(t+\Delta t/2)} \Delta t \tag{2}$$

where $\dot{u}_i^{(t)}$ and $u_i^{(t)}$ are the velocity and position (respectively) of component i ($i = 1, 3$) at time t , ΣF_i is the sum of all force-components i acting on the node of mass m , with timestep Δt . The angular velocities, ω_i , of component i ($i = 1, 3$) at time t are calculated from the following central difference equations:

$$\omega_i^{(t+\Delta t/2)} = \omega_i^{(t-\Delta t/2)} + \frac{\Sigma M_i^{(t)}}{I} \Delta t \tag{3}$$

where ΣM_i is the sum of all moment-components acting on the node of moment of the inertia, I .

After all nodes have been visited (applying Eq. (1) to each node), a scan of all springs is performed. If a spring is unbroken, the following calculations are performed at time t (time superscript omitted for clarity):

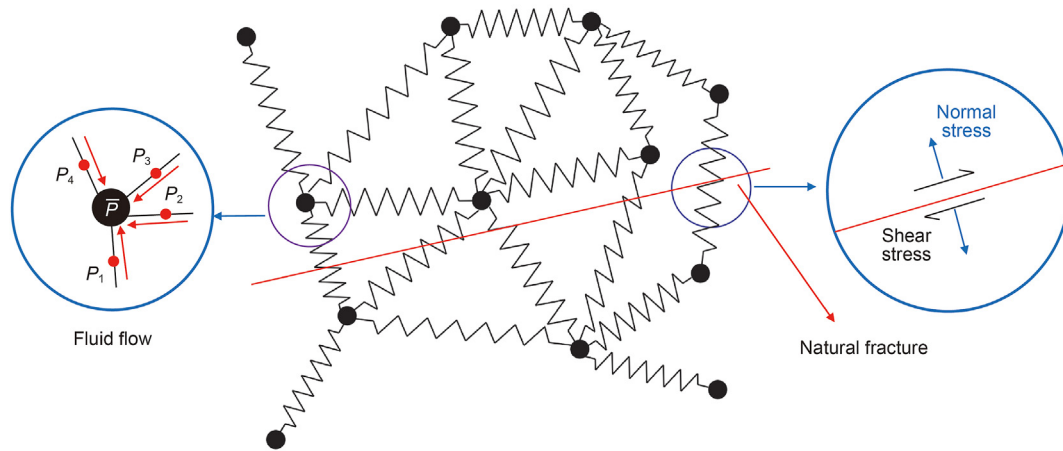


Fig. 3. Schematic of the 3D lattice. The red solid line represents the trace of natural fracture; the circle on the left shows the fluid flow through a node; the circle on the right shows the normal stress and shear stress on a natural fracture.

$$\dot{u}_i^{rel} = \dot{u}_i^A - \dot{u}_i^B \tag{4}$$

where the superscript “rel” denotes “relative”, and “A” and “B” denote the two nodes connected by the spring.

$$\dot{u}^N = \dot{u}_i^{rel} n_i \tag{5}$$

$$\dot{u}_i^S = \dot{u}_i^{rel} - \dot{u}^N n_i \tag{6}$$

where “N” denotes “normal”, “S” denotes shear, n_i is the unit normal vector, and the Einstein summation convention applies to repeated indices. The normal and shear forces then are updated:

$$F^N \leftarrow F^N + \dot{u}^N k^N \Delta t \tag{7}$$

$$F_i^S \leftarrow F_i^S + \dot{u}_i^S k^S \Delta t \tag{8}$$

where k^N and k^S are the spring normal and shear stiffnesses, respectively. Finally, the new spring forces are added (with the appropriate signs) to the force-sums of the associated nodes:

$$\Sigma F_i^A \leftarrow \Sigma F_i^A - F^N n_i - F_i^S \tag{9}$$

$$\Sigma F_i^B \leftarrow \Sigma F_i^B + F^N n_i + F_i^S \tag{10}$$

For a regular spring (part of the intact rock material), the vector n_i is the unit normal from node A to node B.

3.3. Fracture propagation

In order to accurately describe the initiation and propagation of hydraulic fractures, the SJM algorithm is applied to the lattice algorithm. SJM algorithm allows slip and separation between particles in contact, representing shear failure and tensile failure of cracks in rocks. Under the condition of tension, the normal stress on a spring is considered positive and used to indicate whether a fracture is open: when the normal stress is greater than the tensile strength of the spring, it appears as the elastic failure and fracture opening; when the normal stress is compressive, the shear stress in the fracture is mainly related to the maximum friction following the expression:

$$\text{when } F^N > F^{Nmax}, \text{ then } F^N = 0, F_i^S = 0 \tag{11}$$

$$\text{when } |F_i^S| > \mu |F^N|, \text{ then } |F_i^S| \leftarrow F_i^S \frac{\mu |F^N|}{|F_i^S|} \tag{12}$$

where μ is the friction coefficient of the joint segment.

3.4. Fluid flow formulation

In the 3D lattice algorithm, the flowing fluid comes from two sources: the fluid produced by prefabricated fractures and neutralized lattice springs. The fluid in fractures and in the matrix is solved by means of fluid nodes that are connected by pipes. The flow in fractures is solved using the flow model geometry, which consists of a network of fluid nodes and pipes. The fluid flow in matrix, which is a function of permeability, fluid storage, and fluid leak-off, uses the pore pressure stored in the springs of the solid model. Fluid is exchanged between the fractures and matrix. The fluid pressures are stored in the fluid nodes that act as penny-shaped microcracks located at the broken springs or springs intersected by the pre-existing joints.

It is assumed that the pipe width (in the joint plane) is equal to its length. The flow rate along a pipe, from fluid node A to node B, is calculated based on the following relation:

$$q = \beta k_r \frac{a^3}{12\mu} [p^A - p^B + \rho_w g (z^A - z^B)] \tag{13}$$

where a is the hydraulic aperture, μ is the fluid viscosity, p^A and p^B are the fluid pressures at nodes A and nodes B, respectively, z^A and z^B are elevations of nodes A and B, respectively, and ρ_w is the fluid density. The relative permeability, k_r , is a function of saturation, s :

$$k_r = s^2 (3 - 2s) \tag{14}$$

3.5. Hydro-mechanical coupling

In the lattice model, the fluid-solid coupling is mainly manifested in the changes of fracture opening. When the fluid pressure is increased, rock deformation increases and eventually fractures are initiated. Fracture permeability depends on aperture or on the

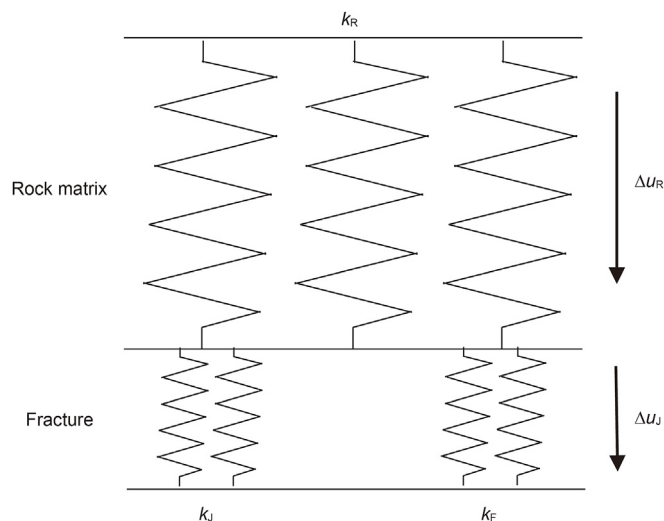


Fig. 4. Diagram of displacement and stiffness in crack normal direction.

deformation of the solid model. As fractures propagate, fracture openings lead to increased filtration loss of the fracturing fluid, which in turn reduces fluid pressure and restricts the expansion of hydraulic fractures. Considering the displacement of node elements, the stiffness of the whole rock must be considered in three aspects: crack, fluid, and matrix. Fig. 4 illustrates the mechanical arrangement in the normal direction. The combined joint normal stiffness, k_C :

$$k_C = k_J + k_F \tag{15}$$

where k_J is the normal stiffness of fracture, k_F is the normal stiffness of fluid.

The total element stiffness, k_T :

$$k_T = \frac{k_R k_C}{k_R + k_C} \tag{16}$$

where k_R is the normal stiffness of rock matrix.

The displacement of nodes can be obtained by using generalized Hooke's law (Batchelor, 2000). Then the force of nodes and elastomers is obtained. Finally, the opening of cracks is determined. In this way, the full coupling of the lattice algorithm is realized.

4. Numerical model

4.1. Simulation schemes and cases

According to representative logging data (Fig. 5), the main coal seams in the Lin-Xing area are often mixed with mudstone and sandstone. Commingling production of coalbed methane and tight sandstone gas in adjacent thin layers are often desirable. Typically, the formation combinations can be represented by three scenarios: 1) a thick section of coal seam sandwiched by sandstones; 2) a thin coal seam layer overlay by gas-bearing tight sandstone; 3) two coal seams separated by a thin layer of sandstone. Accordingly, we designed three numerical simulation schemes as follows:

- Scheme 1: sandstone-coal-sandstone
- Scheme 2: sandstone (dry and gas-bearing layers)-coal-mudstone

- Scheme 3: sandstone-coal-sandstone-coal-sandstone

The schematic diagrams of the combination of the three simulation schemes are shown in Fig. 6. In all simulation schemes, models are set up as cubes of 40 m in length. The specific layer thickness is scaled according to the actual logging data. The location of clustering perforation is selected in gas-bearing coal measure or sandstone strata. To provide input parameters for the simulation, laboratory experiments were conducted on core samples from sandstone, coal, and mudstone formations (Table 1). Rock mechanical parameters, such as Young's modulus, Poisson's ratio, tensile strength, compressive strength, cohesion, and friction angle were measured. Combined with logging curves, the magnitude and direction of *in-situ* stress were measured through Kaiser acoustic emission technique. The selection of fracturing parameters is based on the well data which are shown in Table 2. Numerical model fixed displacement boundary to prevent rigid rotation. The initial perforation aperture is assumed to be 0.1 mm. The simulation is initially run in the mechanical mode for 0.1 s to achieve the initial model equilibrium. Simulation continues in the hydro-mechanical coupling mode, as fluid is injected into the perforation node at a constant rate.

Under the three simulation schemes, we designed simulation cases to systematically study the effects of perforation location and lengths on fracturing performance (Table 3). In Scheme 1, logging data shows that the thickness of the coal seam is about 10 m, and the upper and lower formations are thick sandstones. Therefore, the model is set up with a 10-m-thick coal seam sandwiched by two 15-m-thick sandstone layers. Because the middle coal seam is the only gas-bearing layer, the location and length of perforation are only considered in the coal seam. Perforation location is set in the upper or middle part of the coal seam with lengths varying from 3 to 9 m.

In Scheme 2, the upper sandstone layer contains a dry section 15-m thick and a gas-bearing section of 5-m thick; the middle part is a thin coal seam 4.7-m thick; and the lower part is a 15-m thick mudstone layer. In order to maximize gas production, the coal seam and gas-bearing sandstone layer are fractured together. The sandstone layer is fully perforated, whereas the middle coal seam is perforated by different lengths from 1 to 5 m.

In Scheme 3, the coal seam consists of a thick coal seam of 11.2-m thick and a thin coal seam 2.8-m thick which are separated by a thin sandstone layer 4.8-m thick. This scheme simulates the scenario of two coal seams sandwiched by thin sand beds. For the perforation, the optimal case is that the fracture propagates through the upper thin coal seam to realize indirect fracturing. To help achieve indirect fracturing, perforation location is set at the top or the upper part of the thick coal seam with lengths varying from 3 to 7 m.

4.2. Model verification

In order to quantitatively evaluate the reliability of the discrete lattice method for simulating hydraulic fracture propagation, the numerical solution of two-dimensional penny-shaped fracture is compared with the theoretical solution proposed by Dontsov (2017). Based on the parameters in Table 4, a square model with a side length of 1 m was established, and an annular crack with a radius of 0.01 m was prefabricated in the middle of the model. It should be emphasized that since the influence of confining pressure is not taken into account in the theoretical solution, no confining pressure is loaded in the numerical model. The comparison results of numerical and theoretical solutions of the model are

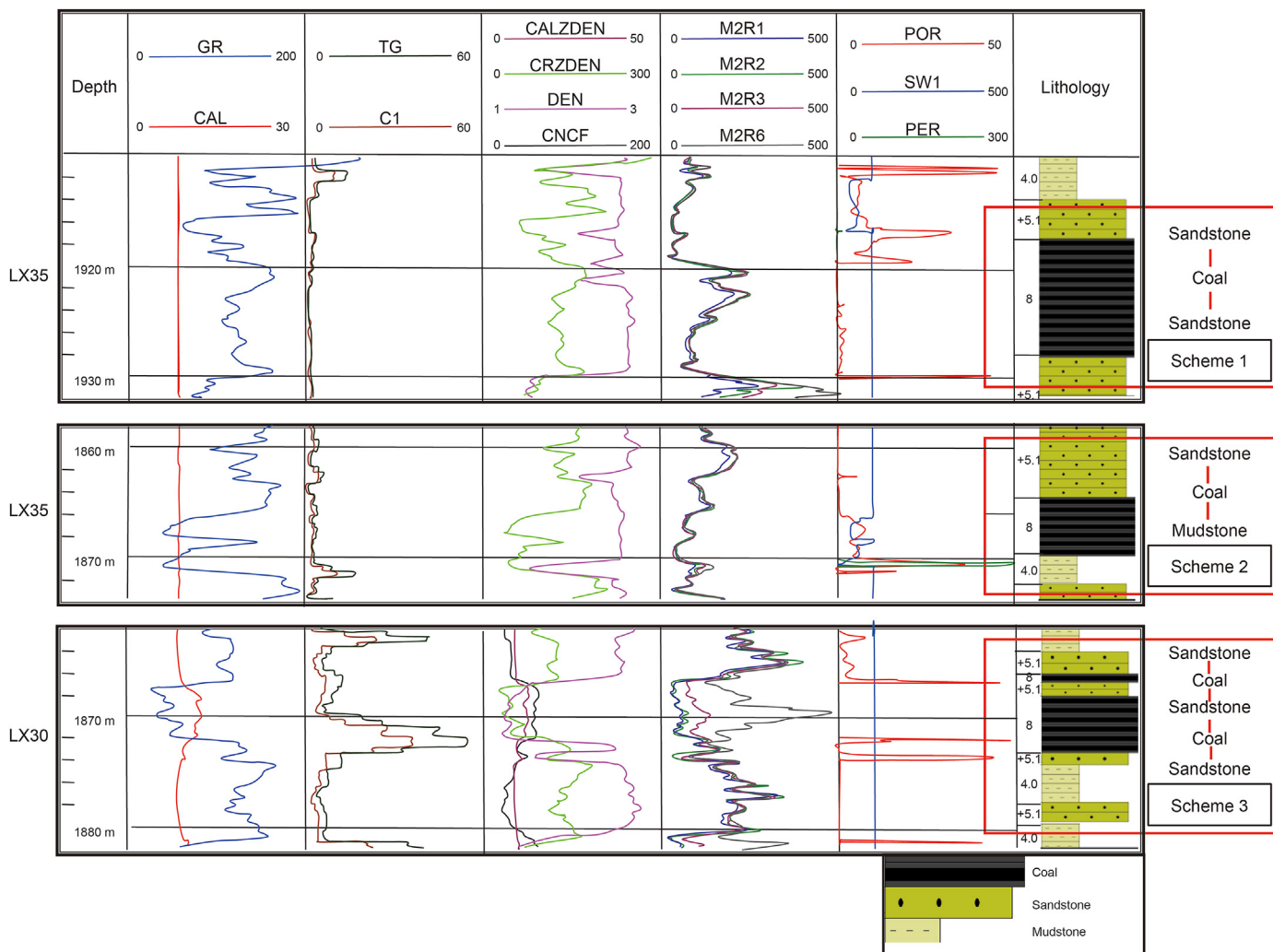


Fig. 5. Typical logging curves and stratigraphic combinations in the Lin-Xing block.

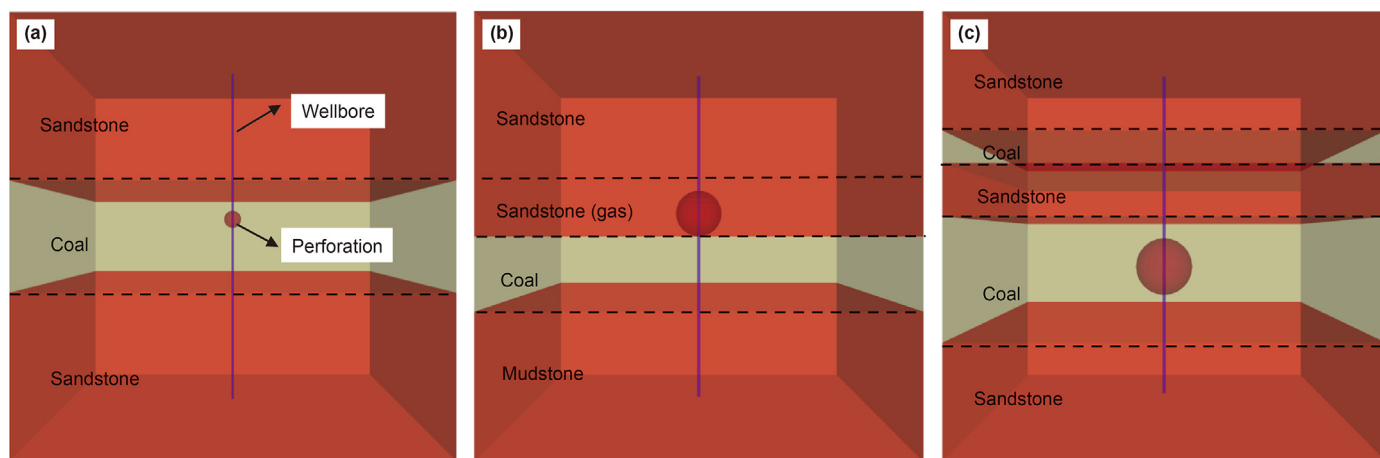


Fig. 6. Schematic diagrams of the three simulation schemes. Each scheme is modeled by a cube of 40 m × 40 m × 40 m in size; the purple lines show the wellbore; the centre of the red ball is the injection point and the size of the red ball represents the length of the perforation along the wellbore.

Table 1
Rock mechanics parameters of numerical models in the Lin-Xing block.

Rock	Young's modulus, GPa	Poisson's ratio	Density, g/cm ³	Tensile strength, MPa	Compressive strength, MPa	Cohesion, MPa
Sandstone	17	0.2	2.5	3.5	50	6
Coal	1.4	0.3	1.8	1	15	2
Mudstone	25	0.23	2.8	4.6	65	7

Rock	Frictional angle, degree	Permeability, mD	Porosity	σ_v , MPa	σ_H , MPa	σ_h , MPa
Sandstone	60	0.28	6.50%	45	38.7	33.5
Coal	10	2	6%	45	33	29.2
Mudstone	120	0.19	5.60%	45	42	37

Table 2
Fracturing parameters of numerical models in Lin-Xing block.

Injection rate, m ³ /s	Fluid viscosity, mPa·s	Fluid density, g/cm ³	Perforation phase angle, degree	Perforation density, m	Perforation diameter, in
0.05	3	1.08	60	16	0.453

Table 3
Perforation parameters for three simulation schemes.

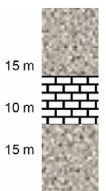
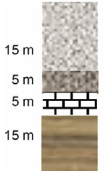
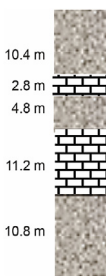
Stratigraphic combination	Number	Central position of perforation (from the roof), m	Perforation length, m
	#1-1	3	3
	#1-2	3	6
	#1-3	5	3
	#1-4	5	6
	#1-5	5	9
	#2-1	0.5	1
	#2-2	1	2
	#2-3	1.5	3
	#2-4	2	4
	#2-5	2.5	5
	#3-1	0	3
	#3-2	0	5
	#3-3	2	3
	#3-4	2	5
	#3-5	2	7
	#3-6	4	5
	#3-7	4	7

Table 4
Parameters of the numerical model.

Parameters	Value
Horizontal maximum principal stress, MPa	3
Horizontal minimal principal stress, MPa	2
Vertical stress, MPa	3
Tensile strength, MPa	3.5
Cohesion, MPa	6
Compressive strength, MPa	50
Fracture toughness, MPa m ^{0.5}	0.5
Yong's modulus, GPa	17
Poisson ratio	0.2
Injection rate, m ³ /s	0.05
Fluid viscosity, mPa s	3

shown in Fig. 7b. The fracture width and length of numerical simulation are in good agreement with the theoretical calculation results. To further verify the accuracy of the model, strain controlled pull-out test was used to test the fracture toughness of the numerical model and compare it with the basic fracture toughness data. A tensile model with a side length of 1 m was established, and an initial fracture of 0.5 m was prefabricated in the middle of the model (Fig. 7c). The fracture toughness is calculated by the following formula (Bunger et al., 2012). The calculation result of fracture toughness is 0.494 MPa m^{0.5}. The calculated results are very close to the actual fracture toughness, so the numerical model can accurately simulate fracture propagation. Combining the verification results of the above two methods, the numerical model

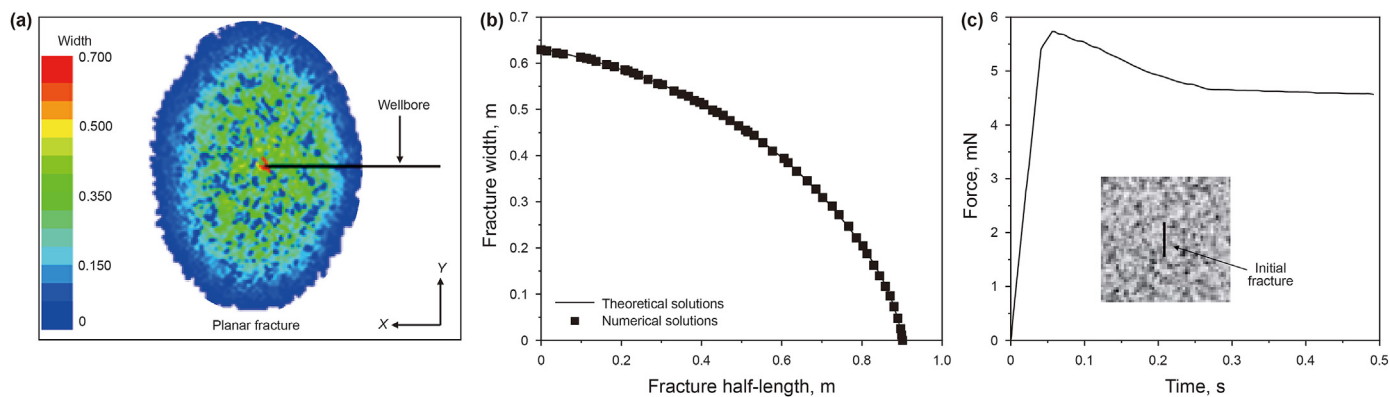


Fig. 7. Numerical model validation results. (a) Penny-shaped fracture morphology. (b) Comparison between numerical and theoretical solutions of fracture length and width. (c) Fracture tensile curve of numerical model.

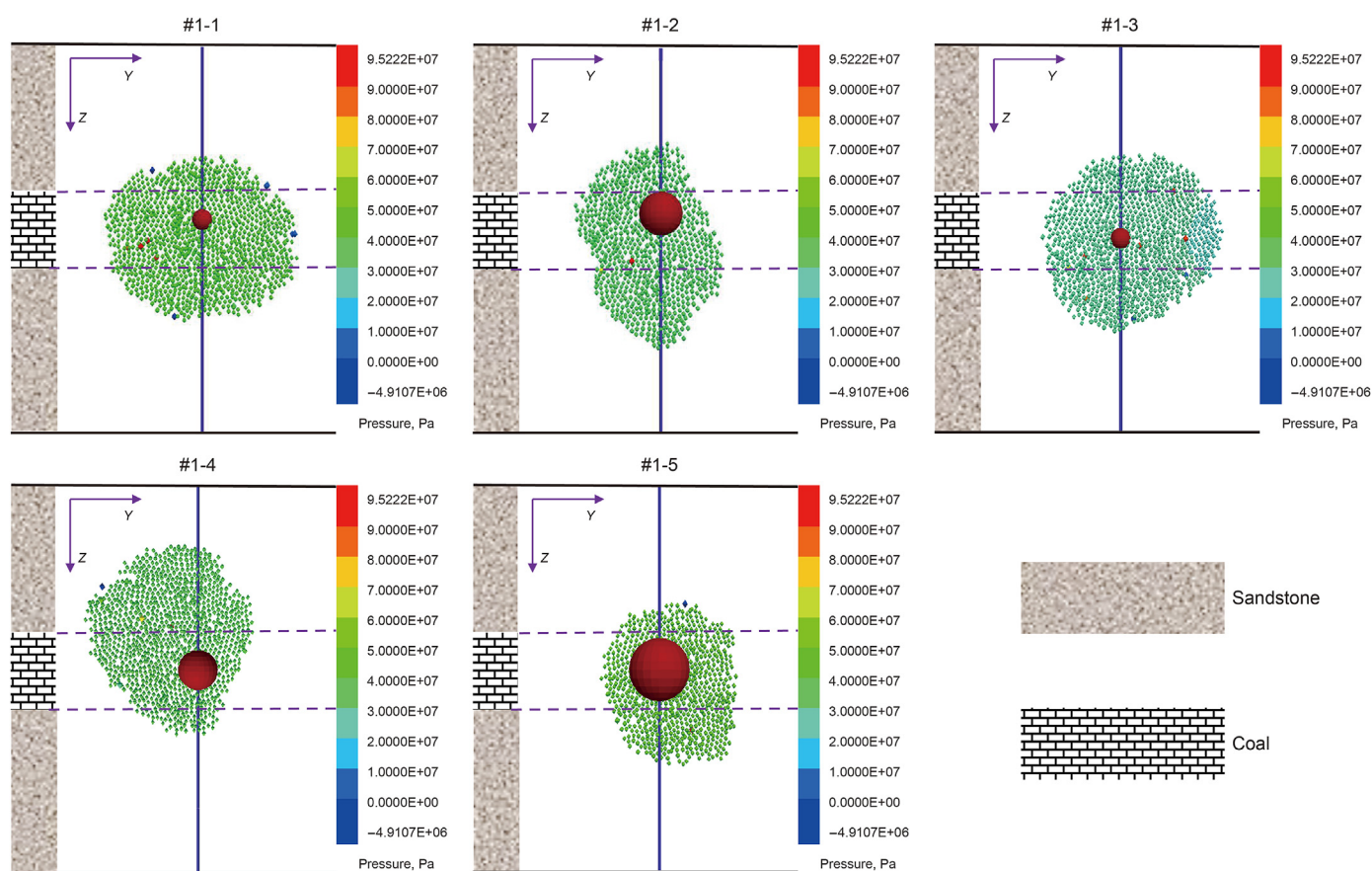


Fig. 8. Simulation results of Scheme 1 with different perforation positions and lengths. The left side represents the stratigraphic combinations; the center section shows the fracture propagation area; the right side shows the legend of fluid pressure.

established by the discrete lattice method can accurately and qualitatively describe the geometry of hydraulic fractures.

$$K_{IC} = \sigma \sqrt{\pi L} \left[\sec \left(\frac{\pi L}{2W} \right)^{0.5} \right] \left[1 - 0.025 \left(\frac{L}{W} \right)^2 + 0.06 \left(\frac{L}{W} \right)^4 \right] \quad (17)$$

where K_{IC} is the fracture toughness, σ is the fracture stress, W is the prefabricated fracture length, and L is the model side length.

5. Numerical simulation results and analysis

5.1. Fracture areal extension

Fracture areal extension for Scheme 1 is shown in Fig. 8. Comparing between different cases, lateral and vertical fracture extension are strongly affected by perforation lengths but not perforation location. Small perforation length (#1-1 & #1-3) leads to similar lateral and vertical fracture extension, whereas intermediate perforation length (#1-2 & #1-4) results in greater vertical

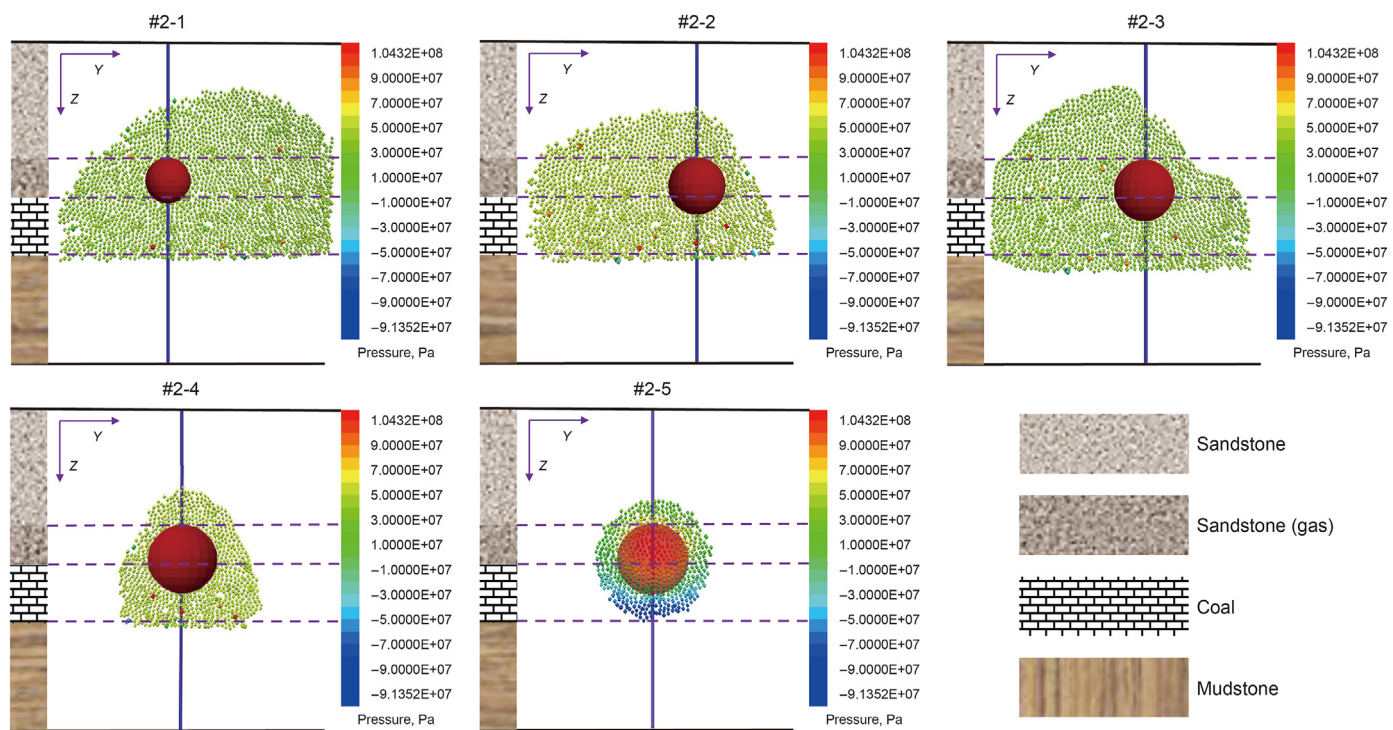


Fig. 9. Simulation results of Scheme 2 with different perforation positions and lengths. The left side represents the stratigraphic combinations; the center section shows the fracture propagation area; the right side shows the legend of fluid pressure.

extension. For large perforation length (#1-5), fracture area is noticeably reduced. On the one hand, this is due to that the bottom hole pressure decreases with the increase in the discharge area given the same fluid injection rate. This phenomenon is particularly noticeable in coal seams with well-developed coal cleats. On the other hand, fluid filtration becomes more significant with the increase in perforation length. These two factors lead to a complex fracture morphology near the wellbore in the coal seam. Therefore, the influence of perforation section length on fracturing coal seam is expected to be stronger than that in other rocks. Comparing to perforation lengths, whether perforating in the upper or middle part of the coal seam does not seem to significantly affect fracture areal extension.

Scheme 2 allows us to investigate the competition of fracture propagation in the two adjacent sandstone and coal seam layers as shown in Fig. 9. When both the sandstone and coal seam are perforated, the fracture tends to initiate from the coal seam because of the smaller fracture toughness and lower *in-situ* stress. Then the pressure is raised near the wellbore because of the low flow conductivity caused by the fracture complexity. As the pressure continues to rise, fracture then initiates in sandstone. When the fracture extends vertically to the lower mudstone layer, it is blocked due to the stress barrier effect of the mudstone. As the sandstone has greater brittleness, the fractures begin to propagate through the sandstone layer. Our simulation shows that, when the perforation length in coal seam is small (#2-1, #2-2, #2-3), the fracture area is relatively large and comparable; when the perforation length is large (#2-4 & #2-5), the fracture area is much smaller, which is due to reduced bottom hole pressure as shown in Scheme 1.

Fracture extension for Scheme 3 is shown in Fig. 10. When setting the perforation central point at the interface of sandstone and coal (#3-1, #3-2), small perforation segment is better for fracture vertical extension through the upper thin layer. When the

perforation central point is 2 m below the roof of the thick coal seam (#3-3, #3-4, #3-5), the fractures connect the upper thin coal seam when the length of perforation segment is 5 m. When the perforation section is in the middle of the thick coal seam (#3-6, #3-7), fractures in both scenarios of the 5 and 7 m perforation length extend to the upper thin coal seam. Scheme 3 shows that the perforation is best located in the middle-upper part of the thick coal seam with medium to long length perforation sections.

5.2. Fracture height

When fracturing multi-layers, it is often difficult to control fracture height. In a single coal seam, it is necessary to control the height extension as shown in Scheme 1. When multiple layers are combined, indirect fracturing of small layers help improve total production. As shown in Scheme 3, fractures can penetrate the interlayer and reach to the upper thin coal seam to achieve indirect fracturing when initiating fracture in the thick coal seam. When the upper and lower formations have different lithologic properties, the fractures will have different results as shown in Scheme 2. The results of fracture height of the three schemes are shown in Fig. 11.

We studied the effects of perforation location and perforation length on fracture extension through layers. When perforating in a single coal seam, its vertical expansion reduces with the increase in perforation length, as shown in #1-4 and #1-5 (Fig. 11a). Perforation in the middle-upper part of the coal seam is better than that in the middle part. Considering the fracturing fluid friction, when the fractures expand along the direction of height, the influence of the perforation length is significant because of the cleats and natural fractures in coal. Under the condition of commingling production of sandstone gas and coalbed gas, it is not ideal to perforate all the sandstone layers as did in the field, because it is difficult to control the fracture height in multi-layers as shown in #2-5 (Fig. 11b). The control of fracture height in mudstone is very effective, this is

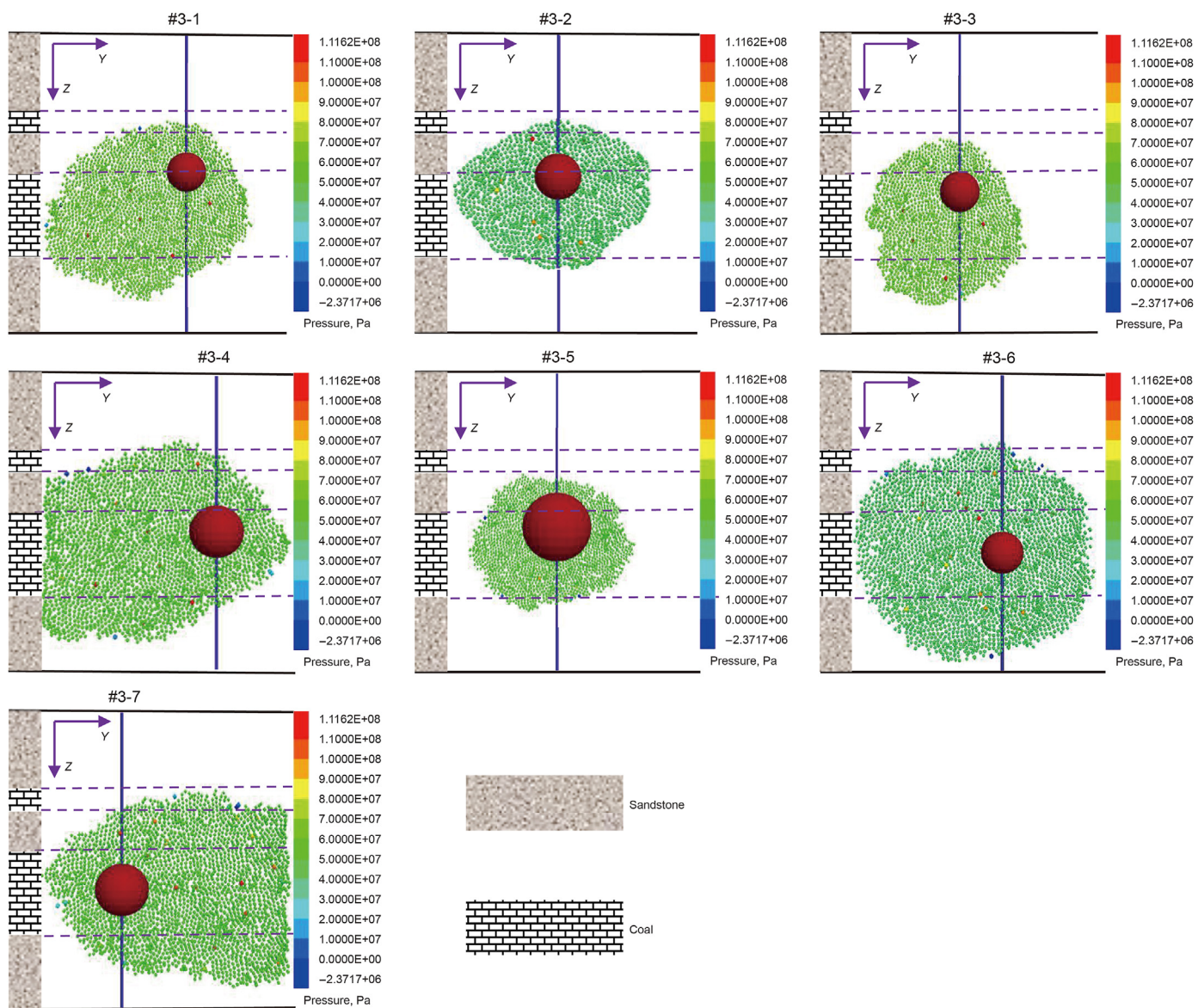


Fig. 10. Simulation results of Scheme 3 with different perforation positions and lengths. The left side represents the stratigraphic combinations; the center section shows the fracture propagation area; the right side shows the legend of fluid pressure.

because the larger modulus of elasticity and tensile strength of the mudstone makes it difficult for the fracture to penetrate the layer, and the fracture is usually stopped when it extends to the mudstone interface (Guo et al., 2016). With the increase in perforation sections in thin coal seams, vertical expansion in the coal seam does not have much impact. When the multi-layer is fractured at the same time, it is not necessary to open all the lower coal seams. The best stimulation results are #3-1 and #3-5 (Fig. 11c), both have achieved indirect fracturing of thin seams. When perforating at the interface of sandstone and coal seam, as the length of the perforation increases, the extension of fractures in vertical direction decreases significantly.

The strata lithology and well completion scheme have great influence on the vertical extension of hydraulic fractures in multi-layers. When the horizontal stress difference between the upper and lower interlayer is large, there is often an asymmetry growth of fracture height (Fig. 12, Simonson et al., 1978). Previous studies of multi-layers mainly focused on the mechanical properties between

the production layer and the adjacent interlayers. But the asymmetry caused by the stress difference was rarely considered in the fracturing design. The results of this study show that the stress difference between these interlayers should be fully evaluated in the fracturing design. Indirect fracturing on upper and lower thin coal seams can be achieved by using this asymmetric feature. Besides, the extension of fracture in sandstone can be applied to reduce the fracture complexity of coal seam and increase the fracture length and SRV. The numerical schemes in this study show that, whether the fracturing in a single thin coal seam or in a multi-layered medium, shortening the perforation length in coal seam is the main way to increase the gas production.

5.3. Fracture aperture

We choose the simulation Scheme 3 to study the effects of different perforation positions and lengths on fracture aperture in the process of fracture propagation. We set up the coordinate

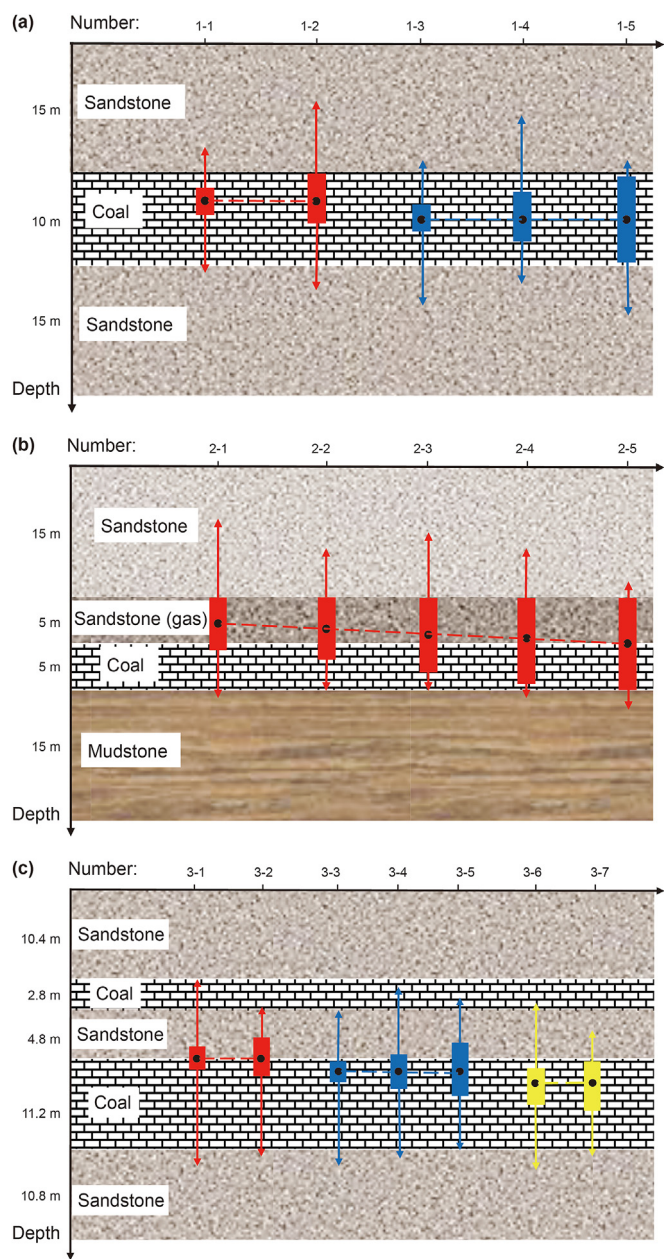


Fig. 11. The fracture heights of three simulation schemes. The black points represent the center point of perforation; the rectangles represent the perforation interval; the arrows indicate the fracture heights.

system by taking the perforation central point as the origin, the length direction of fracture as the Y axis, and the height of fracture as the Z axis. The opening of the fracture along the Y and Z directions is chosen as the fracture aperture (Fig. 13). Cases #3-1 and #3-2 show scenarios that perforating the same length of sandstone and coal seam. Cases #3-4 and #3-5 show scenarios that perforating both in the two layers but more in coal seam than in the sandstone. Cases #3-6, #3-7 correspond to scenarios that perforating only in the thick coal seam. The opening of the simulated fracture in the direction of the fracture height and the seam length is recorded, and a polynomial function is fitted based on the scatter points (Fig. 14). When perforating at the interface between sandstone and coal seam, shorter perforation length results in greater fracture aperture (Fig. 14a and b). When perforating more in the coal seam, fracture aperture appears comparable (Fig. 14c and d).

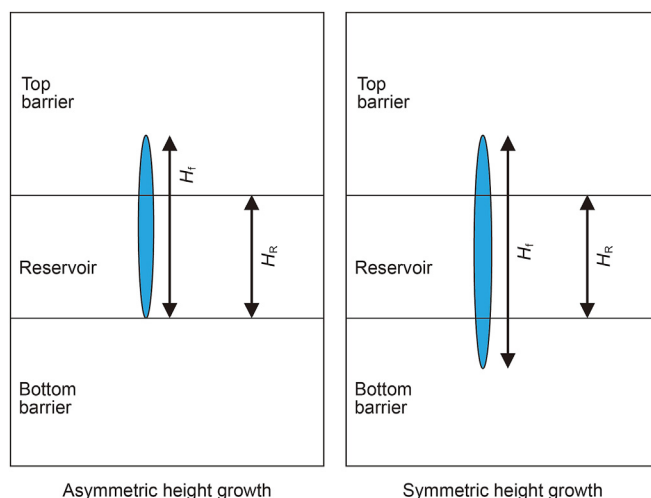


Fig. 12. Two types of hydraulic fracture height growth in a layered medium. Here H_R is the reservoir height and H_f is the overall fracture height (Reprint permission obtained from Simonson et al., 1978).

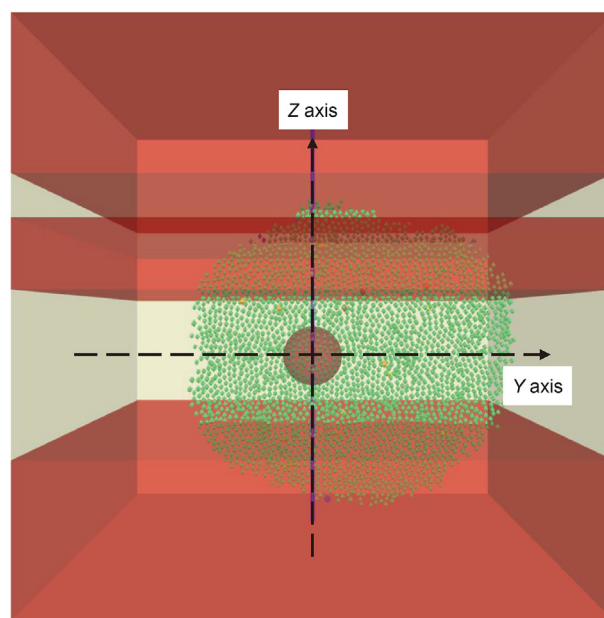


Fig. 13. Coordinate setting in simulation Scheme 3.

However, it leads to asymmetric fracture aperture profile in the length direction (Fig. 14c). When perforating only in the coal seam, shorter perforation length results in greater fracture aperture in the length direction, whereas fracture aperture is more or less similar in the height direction (Fig. 14e and f).

By comparing the different cases in Fig. 14, we arrive at some conclusions for the effects of perforation location. When fractures initiate in soft coal strata, fracture opening becomes more dispersed, which represents the strong non-planarity around the wellbore. This is harmful to the proppant migration. Fig. 15 shows the fracture initiation around the wellbore in a small-scale coal seam model with all perforation tunnels being explicitly represented in which the complex fracture morphology near the wellbore can be seen. Due to the complexity of stress field near the wellbore, stress fields interfere with each other during initiation and propagation of hydraulic fractures. At the same time, because

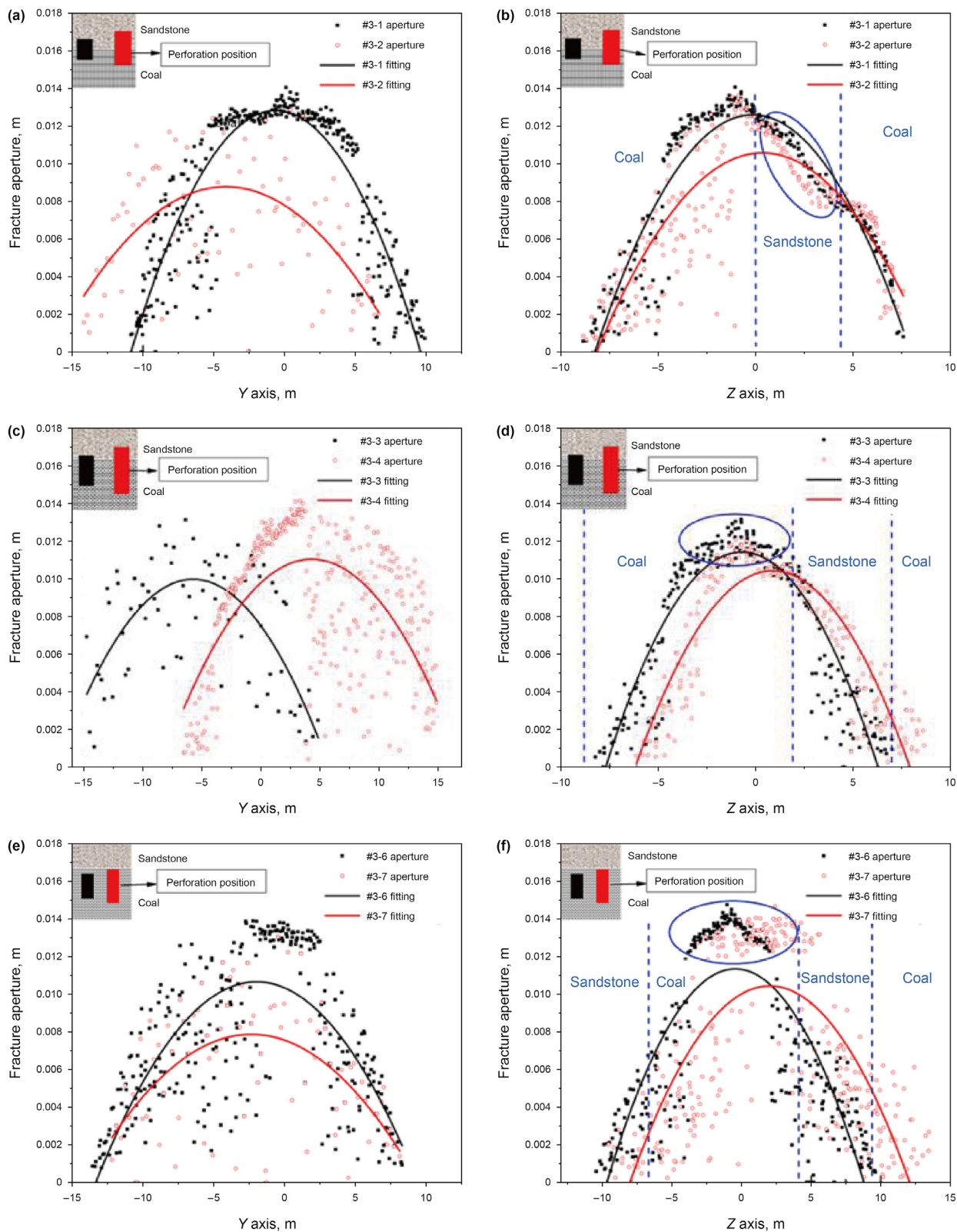


Fig. 14. Fitting of fracture aperture along the Y and Z axes of different perforation schemes in Scheme 3. (a) (c) (e) show the fracture aperture in the Y direction; (b) (d) (f) show the fracture aperture in the Z direction. The blue dotted lines represent the boundaries of each layer.

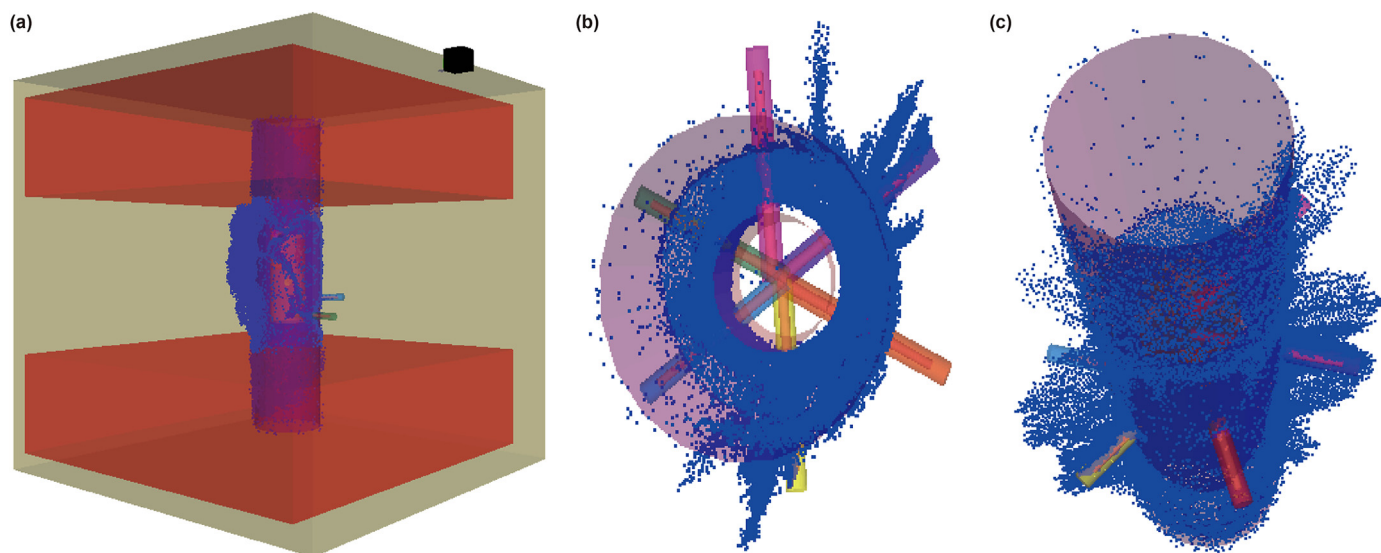


Fig. 15. The simulation results of complex fracture morphology near the wellbore when perforating only in coal seam. (a) Small scale coal seam perforating model; (b) Top view of fracture morphology near the wellbore; (c) Side view of fracture morphology near the wellbore. (The blue dots represent areas of fracture propagation).

of the development of bedding planes and cleat system in the coal seam, the tensile and shear strength of these weak structural planes is much lower than that of the rock matrix, resulting in the initial fracture is easily diverted to the connected weak structural plane. The result is complex fracture morphology in the near-wellbore area. Observing the opening of the fracture in the direction of the height (Z axis) (Fig. 14b, d, f), the fracture aperture in the sandstone is generally less than that in the coal seam. That is because on the one hand, the elastic modulus of the coal rock is less than that of the sandstone, and Poisson's ratio is larger than that of the sandstone. On the other hand, the horizontal stress in the coal seam is often less than the sandstone layer under the same condition of vertical compaction. Greater fracture aperture in the coal seam suggests that proppants are likely easily transported into the coal seam, which is favorable for increasing fracture conductivity and therefore gas production.

6. Discussion

In commingling production of coal measures strata, we need to take the geological and engineering factors into account. The condition of combined production and fracturing construction scheme are determined by considering the real actual formation. The above numerical simulation is the result of the combined production of the typical strata in the Lin-Xing block. If the research results will be widely applied in the field, it is also necessary to discuss the stratigraphic combination, lithological difference, burial depth and gas storage state.

6.1. Stratigraphic combination

The purpose of coal measure strata combined production is to maximize regional production. In the overall development process, it is necessary to classify the production layers according to the lithologic combination and thickness of the strata. In a single coalbed gas formation, for a large section of the coal seam with a thickness of upper and lower sandstone over 5 m (Scheme 1) or an intermediate sandstone stratum with an interlayer of more than 10 m, it is appropriate to extract the gas separately. The coal seam with sandstone on top and mudstone at bottom can be perforated

near the mudstone in the coal seam because of the higher barrier ability of mudstone than sandstone. When there is sandstone gas at the top of the coal seam, most of the sandstone and a small part of adjacent coal rock should be perforated by small perforation section. When a large coal seam is divided into the main thick coal seam and thin coal seam by sandstone interlayer, it should be perforated in the middle-upper part of the main coal seam, and a small part of the perforation in sandstone interlayer, to connect the thin coal seam through indirect fracturing. Besides, the appropriate perforation section length should be set according to the thickness of the layer, too small length of perforation section will make it hard to propagate through the layers, and too long perforation section will contribute to a small stimulation volume.

6.2. Lithologic differences

The macroscopic heterogeneity of stratum is mainly reflected in lithologic difference. The different mechanical properties and fracture characteristics of sandstone, coal stone and mudstone lead to significant differences in fracture initiation pressure and propagation pressure. For the coal seam sandwiched by sandstones, the coal has lower initiation pressure and smaller fracture propagation velocity, which will lead to the fracture formed firstly in the coal seam and later extend quickly in the sandstone. The long fracture in the sandstone will drive the fracture propagation in the coal seam to realize the overall large stimulation area in multi-layers. Therefore, a certain lithology difference is conducive to fracture propagation of the whole formation. But when the rock property is quite different, the gas interference will be much more difficult to control, such as Scheme 2, due to the differences in fracture initiation sequence and propagation velocity. When the coal seam fracture extends to the lower mudstone boundary, the direction of fracture length is better than that of fracture height in coal and sandstone due to the shielding effect of mudstone, resulting in less longitudinal production layer connectivity. In Scheme 3, there are many interbedded layers between sand-coal layers, so the fracture length expansion is also better than the fracture height when perforating in the middle of coal seam. To sum up, perforation should be mainly in sandstone layer and a small part in coal seam to reduce the interference effect, which also achieves favorable the overall

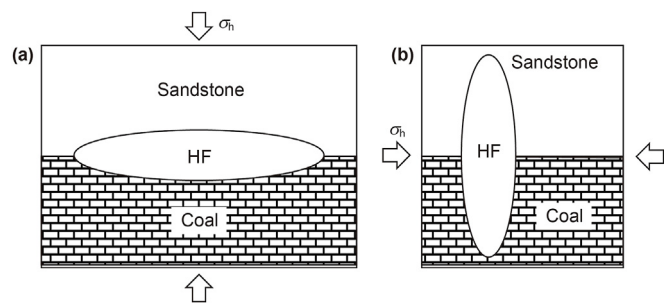


Fig. 16. Schematic diagram of horizontal hydraulic fracture (a) and vertical hydraulic fracture (b) based on different burial depths.

stimulation volume. For the coal seam, the smaller the elastic modulus of the softer coal seam, the smaller the fracture propagation velocity. Besides, cleats are more developed in soft coal seams and the fractures will be more complicated near the wellbore. As a result, if the coal seam is soft, the perforation location should be more inclined to the sandstone interlayer, and smaller perforation length should be used to increase the fracture penetration in the coal seam.

6.3. Burial depth

The buried depth is also a factor affecting the combined production. The direction of fracture propagation in stratum changes with the change of *in-situ* stress. When the stratum depth is shallow, the overburden pressure is the minimum principal stress, where the horizontal fractures will be formed in the coal seam. When the stratum depth is deep, vertical fractures are formed in the coal seam. Therefore, perforation parameters and combined production plan should take burial depth into consideration. In a shallow coal reservoir, single layer mining is the main consideration. Besides, when combined production is needed, perforation point should be set in the interface of sandstone and coal layers because of the horizontal fracture (Fig. 16a). In a deep coal reservoir, for example, the thickness of the coal measure reservoir is more than 1500 m in the Lin-Xing block. The vertical fractures are formed in the coal seam as shown in Fig. 16b. In China, the horizontal fractures in a shallow formation has been mainly studied (Tang et al., 2011), but the deep coal seam combined production remains a major problem, which needs overall consideration in the fracturing.

6.4. Gas storage state

The storage state of coalbed methane also affects the fracturing in multi-layers. There are three states for coalbed methane: adsorbed state, free state and dissolved state, and the first two are dominant. One of the major problems of multi-layer production is the mechanical differences and interference between layers. In the early stage of mining, the coal bed gas flows rapidly and the pore pressure changes rapidly, which may lead to the collapse of the coal seam or sandstone layer. Because the coal bed gas has the characteristic of adsorption, only when the pressure drops to a low state, can the gas flow freely. In commingling production, the coalbed methane can be controlled by controlling the casing pressure of the fracturing section to reduce the interference between coalbed gas and sandstone gas (Qin et al., 2016). According to the production dynamic data of gas in the Lin-Xing block, three modes of curves can be seen (Fig. 17): (a) Sandstone gas and adsorbed coalbed methane coexist, (b) sandstone gas is dominant, (c) sandstone gas and free coalbed methane coexist. In Fig. 17a, there are two peaks in the production rate curve. The first peak represents sandstone gas production, and the second peak indicates that after the pressure drops to the desorption pressure of coalbed methane, a mass of coalbed methane in the adsorbed state is released to reach the second peak in the curve. In Fig. 17b, there is only one peak in the early stage, and then the production drops quickly, which indicates that sandstone gas dominates the production, and a small amount of coalbed methane gas desorption only causes small curve fluctuation. In Fig. 17c, there is also one peak in the curve, but the production descends slowly, which indicates that both the free coal bed methane and sandstone gas start production at the beginning of the early stage. In commingling production of different types of gas, mode 1 is more conducive to combined production because coal bed methane and sandstone gas are not produced at the same time, so the interference is reduced. The mode 3 is the most unfavorable for combined production, because the coalbed methane in the stratum is mainly free state, and the two types of gas will show significant interlayer interference during production due to the large stress difference between layers.

7. Result validation

To verify the accuracy of the numerical simulation results, true tri-axial experiments of sand coal interbedding are conducted. A stratigraphic combination of sandstone interlayers in the thick coal seam is prepared to simulate Scheme 1 (Fig. 18a), Scheme 2 (Fig. 18c) and Scheme 3 (Fig. 19). The rock samples of

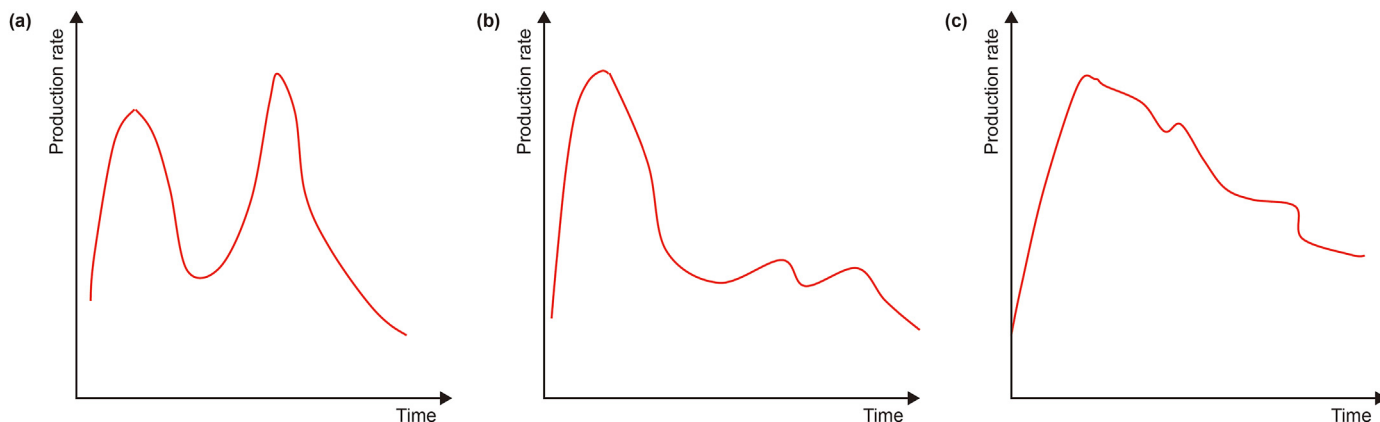


Fig. 17. Three typical production curves in the Lin-Xing block based on different gas storage states. (a) Model 1; (b) Model 2; (c) Model 3.

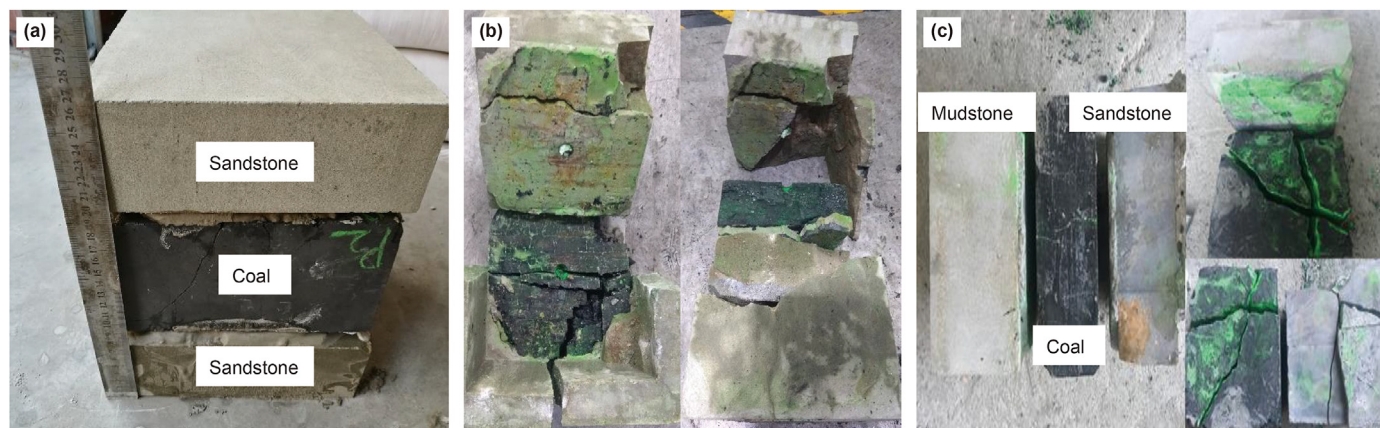


Fig. 18. Laboratory true-triaxial experiment to simulate schemes 1 and 2. (a) Scheme 1: the specimen before fracturing; (b) Scheme 1: fracture morphology after fracturing; (c) Scheme 2: the specimen before fracturing and fracture morphology after fracturing.



Fig. 19. Laboratory true-triaxial experiment to simulate Scheme 3. (a) The specimen before fracturing; (b) and (c) Fracture morphology after fracturing.

300 mm × 300 mm × 300 mm were prepared from large coal and sandstone outcrops in the Lin-Xing block. Besides, cement is used as transition layers between the coal seam and sandstone. The viscosity of fracturing fluid and *in-situ* stresses are selected the same as the numerical simulation.

In Fig. 18a, sandstone, coal seam, and sandstone combination correspond to Scheme 1, where the stress difference between adjacent layers is 4 MPa. The results show that fractures initiated in the coal seam and connected the upper and lower sandstone layers. This experiment verifies the feasibility of perforation fracturing in the coal seam under an interlayer stress difference of 4 MPa to connect sandstone layers, which is consistent with the numerical simulation results. In Fig. 18c, sandstone, coal seam, and mudstone combination correspond to Scheme 2. The results show that fractures in the coal seam are preferentially initiated, followed by fractures in the sand layer. However, the mudstone layer cannot be communicated due to stress barrier. The simulation results of Scheme 2 in Fig. 9 are verified. In Fig. 19a, the thick coal seam, the thin coal seam and the middle sandstone interlayer correspond to #3-7 in Scheme 3, where the perforation is set in the middle part of the coal seam. The experimental results are consistent with the numerical simulation results, indicating that the fractures are not connected to the upper thin coal seam. Due to cleats in the coal seam, a complex fracture network is formed in the coal seam as shown in Fig. 19b and c. In Fig. 19c, there are three main fractures

and multiple secondary joints near the wellbore, which is similar to the results of the numerical simulation.

The eastern part of the LX-101 well section in the Lin-Xing block develops a large section of gas-bearing sandstone layer from 1696 to 1725 m, which contains small sections of thin gas-bearing coal seams in the upper, middle and lower parts. The stratigraphic assemblage falls within Scheme 3 of the study - a large section of sandstone interspersed with a small section of gas-bearing coal seam. The coal seam of this formation is thin, and the multi-gas co-production can be achieved by indirectly fracturing the small coal seam in the surrounding area through perforation in the large sandstone layer. By analyzing the anisotropy changes before and after the casing, the fracturing effect of the fracture interval can be evaluated and the height of fracture propagation can be monitored. After the first fracturing, the anisotropy of the upper and lower coal seams increased, and the upper part of the sand body was completely fractured with obvious changes in the time difference between fast and slow transverse waves, but the intermediate dry layer was not completely fractured, so the effective range of fracturing height was 1700.7 to 1716.5 m (Fig. 20). After the second fracturing, the anisotropy of the lower part of the fractured section increased significantly and the fractures extended to the upper and lower sections, so the upper part of the sand body of the original fractured section and the intermediate dry layer were significantly transformed by the fracturing. The fracture penetrates the layer

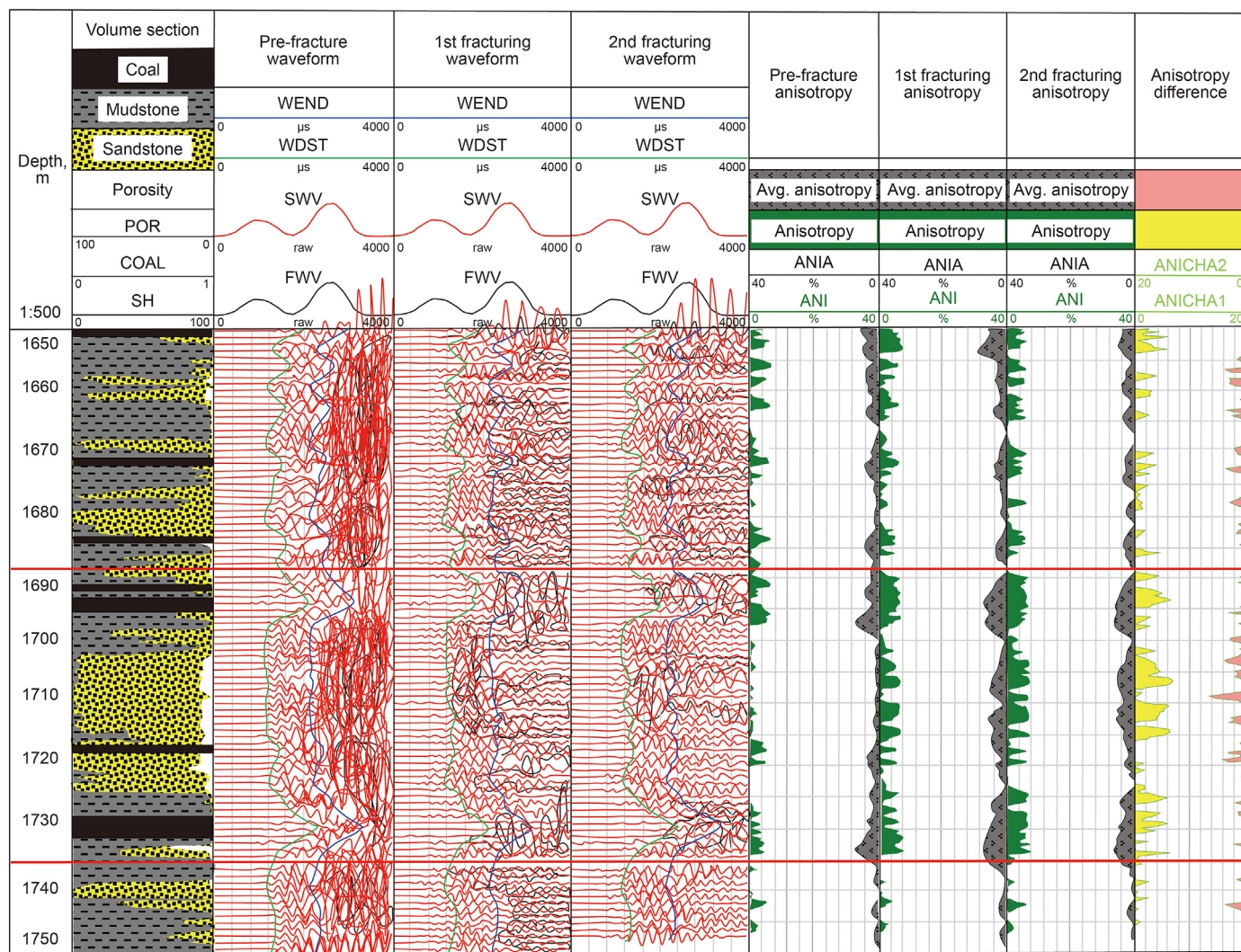


Fig. 20. Changes in transverse wave time difference and anisotropy before and after hydraulic fracturing in well LX-101.

vertically and communicates with a small section of coal seam, realizing multi-gas co-production.

8. Conclusions

We performed a numerical simulation study to investigate the effects of different perforation scenarios on hydraulic fracture propagation in coal measure strata of the Lin-Xing block, China. Based on field data, we employed 3D lattice algorithm to simulate three lithologic combinations: 1) a thick section of coal seam sandwiched by sandstones; 2) a thin coal seam layer overlay by gas-bearing tight sandstone; 3) two coal seams separated by a thin layer of sandstone. Our simulation shows the following:

- (1) Perforation position and length in multi-layer reservoirs play a major role in hydraulic fracture propagation. Achieving maximum SRV requires consideration of lithologic sequence, coal seam thickness, stress states, and rock properties.
- (2) To increase the gas production and improve fracturing efficiency, it is possible to simultaneously stimulate coal seam and adjacent gas-bearing sandstones or two coal seams separated by a thin layer. In these cases, perforation location

and length also significantly impact fracture propagation, and therefore should be carefully designed.

- (3) The simulation results using 3D lattice algorithm are qualitatively consistent with laboratory physical simulation. 3D lattice models can be used to effectively simulate the fracture propagation through layers in coal measure strata.

Acknowledgments

The authors are grateful for the financial support by the National Key Research and Development Program of China (Grant No. 2020YFC1808102) and the Natural Science Foundation of China (No. 51874328 and No. 52074311). The authors would like to thank Itasca Consulting Group, Inc. for providing the 3D lattice algorithm software XSite.

References

Adeyeye, A., Perez, R., Boyer, M., et al., 2013. Multizone tight gas completions in the Piceance Basin: over a decade of learnings. In: IPTC International Petroleum Technology Conference. <https://doi.org/10.2523/IPTC-17129-MS>.
 Anderson, G.D., 1981. Effects of friction on hydraulic fracture growth near unbonded interfaces in rocks. SPE J. 21 (1), 21–29. <https://doi.org/10.2118/8347-PA>.
 Batchelor, G.K., 2000. An Introduction to Fluid Dynamics. Cambridge University Press.

- Beugelsdijk, L., De, P.C., Sato, K., 2000. Experimental hydraulic fracture propagation in a multi-fractured medium. In: SPE Asia Pacific Conference on Integrated Modelling for Asset Management. <https://doi.org/10.2118/59419-MS>.
- Bunger, A.P., Zhang, X., Jeffery, R.G., 2012. Parameters affecting the interaction among closely spaced hydraulic fractures. SPE J. 17 (1), 292–306. <https://doi.org/10.2118/140426-PA>.
- Chen, Z., Yang, Z., Wang, M., 2018. Hydro-mechanical coupled mechanisms of hydraulic fracture propagation in rocks with cemented natural fractures. J. Petrol. Sci. Eng. 163, 421–434. <https://doi.org/10.1016/j.petrol.2017.12.092>.
- Damjanac, B., Cundall, P., 2015. Application of distinct element methods to simulation of hydraulic fracturing in naturally fractured reservoirs. Comput. Geotech. 71, 283–294. <https://doi.org/10.1016/j.compgeo.2015.06.007>.
- Damjanac, B., Detournay, C., Cundall, P.A., 2016. Application of particle and lattice codes to simulation of hydraulic fracturing. Comp. Part. Mech. 3 (2), 249–261. <https://doi.org/10.1007/s40571-015-0085-0>.
- Daneshy, A., 1978. Hydraulic fracture propagation in layered formations. SPE J. 18 (1), 33–41. <https://doi.org/10.2118/6088-PA>.
- Dontsov, E.V., 2017. An approximate solution for a plane strain hydraulic fracture that accounts for fracture toughness, fluid viscosity, and leak-off. Int. J. Fract. 205 (2), 221–237. <https://doi.org/10.1007/s10704-017-0192-4>.
- Fang, Y., Han, Y., 2018. Micromechanical modeling of multi-cluster hydraulic fracturing in horizontal well. In: SPE/AAPG/SEG Unconventional Resources Technology Conference. <https://doi.org/10.15530/URTEC-2018-2900577>.
- Feng, Y.C., Gray, K.E., 2016a. A parametric study for wellbore strengthening. J. Nat. Gas Sci. Eng. 30, 350–363. <https://doi.org/10.1016/j.jngse.2016.02.045>.
- Feng, Y.C., Jones, J.F., Gray, K.E., 2016b. A review on fracture-initiation and-propagation pressures for lost circulation and wellbore strengthening. SPE Drill. Complet. 31 (2), 134–144. <https://doi.org/10.2118/181747-PA>.
- Fisher, M.K., Wright, C., Davidson, B., et al., 2002. Integrating fracture mapping technologies to optimize stimulations in the Barnett Shale. In: SPE Annual Technical Conference and Exhibition. <https://doi.org/10.2118/77441-PA>.
- Grassl, P., Fahy, C., Gallipoli, D., et al., 2014. On a 2D hydro-mechanical lattice approach for modelling hydraulic fracture. J. Mech. Phys. Solid. 75, 104–118. <https://doi.org/10.1016/j.jmps.2014.11.011>.
- Guo, J., Zhao, X., Zhu, H., et al., 2015. Numerical simulation of interaction of hydraulic fracture and natural fracture based on the cohesive zone finite element method. J. Nat. Gas Sci. Eng. 25, 180–188. <https://doi.org/10.1016/j.jngse.2015.05.008>.
- Guo, J.C., Luo, B., Zhu, H.Y., et al., 2016. Multilayer stress field interference in sandstone and mudstone thin interbed reservoir. J. Geophys. Eng. 13 (5), 775. <https://doi.org/10.1088/1742-2132/13/5/775>.
- He, W., Liu, J., Xie, D., 2014. Numerical study on fatigue crack growth at a web-stiffener of ship structural details by an objected-oriented approach in conjunction with ABAQUS. Mar. Struct. 35, 45–69. <https://doi.org/10.1016/j.marstruc.2013.12.001>.
- Hou, B., Chen, M., Wang, Z., et al., 2013. Hydraulic fracture initiation theory for a horizontal well in a coal seam. Petrol. Sci. 10 (2), 219–225. <https://doi.org/10.1007/s12182-013-0270-9>.
- Ivares, D.M., Pierce, M., DeGagné, D., et al., 2008. Anisotropy and scale dependency in jointed rock-mass strength—a synthetic rock mass study. In: Proceedings of the 1st International FLAC/DEM Symposium on Numerical Modeling, pp. 231–239.
- Li, L., Liang, Z., Li, G., et al., 2010. Three-dimensional numerical analysis of traversing and twisted fractures in hydraulic fracturing. Chin. J. Rock Mech. Eng. 29 (S1), 3208–3215. CNKI:SUN:YSLX.0.2010-S1-090 (in Chinese).
- Li, D., Zhang, S., Zhang, S., 2014. Experimental and numerical simulation study on fracturing through interlayer to coal seam. J. Nat. Gas Sci. Eng. 21, 386–396. <https://doi.org/10.1016/j.jngse.2014.08.022>.
- Li, Q., Xing, H., Liu, J., et al., 2015. A review on hydraulic fracturing of unconventional reservoir. Petrol. Times 1 (1), 8–15. <https://doi.org/10.1016/j.petlm.2015.03.008>.
- Li, H., Zou, Y., Valko, P.P., et al., 2016. Hydraulic fracture height predictions in laminated shale formations using finite element discrete element method. In: SPE Hydraulic Fracturing Technology Conference. <https://doi.org/10.2118/179129-MS>.
- Li, S., Xiong, Y., Lu, Q.J., et al., 2006. A new method & application of production dividing for commingling production in gas reservoir. Inner. Mong. Pet. Ind. 7, 45. CNKI:SUN:NMSH.0.2006-07-045 (in Chinese).
- Owen, D., Leonardi, C., Feng, Y., 2011. An efficient framework for fluid–structure interaction using the lattice Boltzmann method and immersed moving boundaries. Int. J. Numer. Methods Eng. 87 (1–5), 66–95. <https://doi.org/10.1002/nme.2985>.
- Pierce, M., Cundall, P., Potyondy, D., et al., 2007. A synthetic rock mass model for jointed rock. In: Proceedings of the First CA–US Rock Mechanics Symposium, Vancouver, BC, pp. 341–349.
- Potyondy, D.O., Cundall, P., 2004. A bonded-particle model for rock. Int. J. Rock Mech. Min. 41 (8), 1329–1364. <https://doi.org/10.1016/j.ijrmms.2004.09.011>.
- Qin, Y., Shen, J., Shen, Y.L., 2016. Joint mining compatibility of superposed gas-bearing systems: a general geological problem for extraction of three natural gases and deep CBM in coal series. J. China Coal Soc. 41 (1), 14–23. <https://doi.org/10.13225/j.cnki.jccs.2015.9032> (in Chinese).
- Renshaw, C., Pollard, D., 1995. An experimentally verified criterion for propagation across unbounded frictional interfaces in brittle, linear elastic materials. Int. J. Rock Mech. Min. Sci. Geomech. Abstracts 32 (3), 237–249. [https://doi.org/10.1016/0148-9062\(94\)00037-4](https://doi.org/10.1016/0148-9062(94)00037-4).
- Simonson, E., Abou-Sayed, A., Clifton, R., 1978. Containment of massive hydraulic fractures. SPE J. 18 (1), 27–32. <https://doi.org/10.2118/6089-PA>.
- Sun, Z., Espinoza, D.N., Balhoff, M.T., 2018. Reservoir rock chemo-mechanical alteration quantified by triaxial tests and implications to fracture reactivation. Int. J. Rock Mech. Min. 106, 250–258. <https://doi.org/10.1016/j.ijrmms.2018.04.004>.
- Tan, P., Jin, Y., Han, K., et al., 2017a. Analysis of hydraulic fracture initiation and vertical propagation behavior in laminated shale formation. Fuel 206, 482–493. <https://doi.org/10.1016/j.fuel.2017.05.033>.
- Tan, P., Jin, Y., Han, K., et al., 2017b. Vertical propagation behavior of hydraulic fractures in coal measure strata based on true triaxial experiment. J. Petrol. Sci. Eng. 158, 398–407. <https://doi.org/10.1016/j.petrol.2017.08.076>.
- Tang, S.H., Zhu, B.C., Yan, Z.F., 2011. Effect of crustal stress on hydraulic fracturing in coalbed methane wells. J. China Coal Soc. 36 (1), 65–69. <https://doi.org/10.13225/j.cnki.jccs.2011.01.005> (in Chinese).
- Teufel, L.W., Clark, J.A., 1984. Hydraulic-fracture propagation in layered rock: experimental studies of fracture containment. SPE J. 24 (1), 19–32. <https://doi.org/10.2118/9878-PA>.
- Thallak, S., Rothenburg, L., Dusseault, M., 1991. Simulation of multiple hydraulic fractures in a discrete element system. In: The 32nd US Symposium on Rock Mechanics (USRMS). American Rock Mechanics Association.
- van Eckelen, H., 1982. Hydraulic fracture geometry: fracture containment in layered formations. SPE J. 22 (3), 341–349. <https://doi.org/10.2118/9261-PA>.
- Wang, M., Feng, Y., Wang, C., 2017. Numerical investigation of initiation and propagation of hydraulic fracture using the coupled Bonded Particle–Lattice Boltzmann Method. Compos. Struct. 181, 32–40. <https://doi.org/10.1016/j.compstruc.2016.02.014>.
- Wang, Y.Z., Hou, B., Wang, D., et al., 2021. Features of fracture height propagation in cross-layer fracturing of shale oil reservoirs. Petrol. Explor. Dev. 48 (2), 469–479. [https://doi.org/10.1016/S1876-3804\(21\)60038-1](https://doi.org/10.1016/S1876-3804(21)60038-1).
- Warpinski, N., Teufel, L., 1987. Influence of geologic discontinuities on hydraulic fracture propagation (includes associated papers 17011 and 17074). J. Petrol. Technol. 39 (2), 209–220. <https://doi.org/10.2118/13224-PA>.
- Warpinski, N.R., Mayerhofer, M.J., Vincent, M.C., et al., 2009. Stimulating unconventional reservoirs: maximizing network growth while optimizing fracture conductivity. J. Can. Petrol. Technol. 48 (10), 39–51. <https://doi.org/10.2118/114173-PA>.
- Wu, H., Chudnovsky, A., Dudley, J., et al., 2004. A map of fracture behavior in the vicinity of an interface. Gulf Rocks 2004 the 6th North America Rock Mechanics Symposium (NARMS).
- Xie, Y.G., Guo, L.J., Duan, C.J., et al., 2015. Assessments on potential resources of deep coalbed methane and compact sandstone gas in Linxing Area. Coal Sci. Technol. 43 (2). <https://doi.org/10.13199/j.cnki.cst.2015.02.005> (in Chinese).
- Xing, P., Yoshioka, K., Adachi, J., et al., 2018. Lattice simulation of laboratory hydraulic fracture containment in layered reservoirs. Comput. Geotech. 100, 62–75. <https://doi.org/10.1016/j.compgeo.2018.03.010>.
- Yang, Z.B., Zhang, Z.G., Qin, Y., et al., 2018. Optimization methods of production layer combination for coalbed methane development in multi-coal seams. Petrol. Explor. Dev. 45 (2), 312–320. [https://doi.org/10.1016/S1876-3804\(18\)30034-X](https://doi.org/10.1016/S1876-3804(18)30034-X).
- Zhang, F., Dontsov, E., 2018. Modeling hydraulic fracture propagation and proppant transport in a two-layer formation with stress drop. Eng. Fract. Mech. 199, 705–720. <https://doi.org/10.1016/j.engfracmech.2018.07.008>.
- Zhang, F., Dontsov, E., Mack, M., 2017. Fully coupled simulation of a hydraulic fracture interacting with natural fractures with a hybrid discrete-continuum method. Int. J. Numer. Anal. Model. 41 (13), 1430–1452. <https://doi.org/10.1002/nag.2682>.
- Zhang, F., Wang, X., Tang, M., et al., 2021. Numerical investigation on hydraulic fracturing of extreme limited entry perforating in plug-and-perforation completion of shale oil reservoir in Changqing Oilfield, China. Rock Mech. Rock Eng. 54, 2925–2941. <https://doi.org/10.1007/s00603-021-02450-x>.
- Zhao, H., Wang, X., Liu, Z., et al., 2018. Investigation on the hydraulic fracture propagation of multilayers-commingled fracturing in coal measures. J. Petrol. Sci. Eng. <https://doi.org/10.1016/j.petrol.2018.04.028>.